PHYSICS OF OUR DAYS

Photon entanglement for life-science imaging: rethinking the limits of the possible

A M Zheltikov, M O Scully

Contents

Abstract. Quantum entanglement is a powerful resource that revolutionizes information science, opens new horizons in communication technologies, and pushes the frontiers of sensing and imaging. Whether or not the methods of quantum entanglement can be extended to life-science imaging is far from clear. Live biological systems are eluding quantum-optical probes, proving, time and time again, too lossy, too noisy, too warm, and too wet to be meaningfully studied by quantum states of light. The central difficulty that puts the main roadblock on the path toward entanglement-enhanced nonlinear bioimaging is that the two-photon absorption (TPA) of entangled photons can exceed the TPA of uncorrelated photons only at the level of incident photon flux densities as low as one photon per entanglement area per entanglement time. This fundamental limitation has long been believed to rule out even a thinnest chance for a success of bioimaging with entangled photons. Here, we show that new approaches in nonlinear and quantum optics, combined with the latest achievements in biotechnologies, open the routes toward efficient photon-entanglement-based strategies in TPA microscopy that can help confront long-standing challenges in life-science imaging. Unleashing the full potential of this approach will require, however, high throughputs of virus-construct delivery, high expression efficiencies of genetically encodable fluorescent markers, high-brightness sources of entangled photons, as well as a thoughtful entanglement engineering in time, space, pulse, and polarization modes. We demonstrate that suitably tailored nonlinear optical fibers can deliver entangled photon pairs confined to entanglement volumes many orders of magnitude smaller than the entanglement volumes attainable through spontaneous parametric down-conversion. These ultracompact modes of entangled photons are shown to enable a radical enhancement of the TPA of entangled photons, opening new avenues for quantum entanglement in life-science imaging.

Keywords: nonlinear optics, nonlinear microscopy, quantum optics, bioimaging

A M Zheltikov (1, 2, 3, 4, 5, *), **M O Scully** (2, 6, 7)
(1) International Laser Center, Lomonosov Moscow State University,
   Physics Department,
   Leninskie gory 1, 119991 Moscow, Russian Federation
(2) Institute for Quantum Science and Engineering,
   Department of Physics and Astronomy,
   Texas A&M University, College Station TX 77843, USA
(3) Russian Quantum Center, ul. Novaya 100, 143025 Skolkovo,
   Moscow region, Russian Federation
(4) Tupolev Kazan National Research Technical University,
   KNRTU – KAI, ul. Chetaeva 18, 420126 Kazan, Russian Federation
(5) National Research Center 'Kurchatov Institute',
   pl. Akademika Kurchatova 1, 123182 Moscow, Russian Federation
(6) Princeton University, Princeton, NJ 08544 USA
(7) Baylor University, Waco, TX 76798 USA
E-mail: (*) zheltikov@physics.msu.ru

1. Introduction

Quantum entanglement is one of the cornerstones in the foundation of quantum physics and a powerful resource of rapidly growing quantum technologies [1–4]. Photonics offers a vast arsenal of tools that help engineer and manipulate entangled states of light, providing a unique, highly versatile platform for a practical implementation of advanced quantum concepts, as well as for high-precision experimental tests of the fundamental principles of quantum physics [5–7].

In this remarkable scenery of a blistering progress, there is one high-reward target is always in sight and, yet, is

constantly escaping the frames of quantum optics, staying beyond the reach of its powerful methods. Over many decades, much research has been focused on extending advanced concepts and tools of quantum optics, including quantum entanglement in the first place, to real-life biological applications. With many important discoveries made and significant milestones reached along this way [8], the ultimate goal of these efforts is yet to be achieved. Live biological systems have been constantly eluding quantum-optical probes, proving, time and time again, too lossy, too noisy, too warm, and too wet [9] to be meaningfully studied by quantum states of light.

Quantum imaging [10–20] is on the verge of breaking this spell. Quantum states of light have been shown to enable fundamentally new schemes of microscopy and lithography, providing a spatial resolution well within the diffraction limit [19–22]. When used in a two-photon absorption (TPA) setting, quantum light can drastically modify the behavior of the TPA rate w_2 as a function of the incident photon flux density φ [23–27]. As, perhaps, the most striking manifestation of quantum correlations, in the ultralow-φ regime, the $w_2 \propto \varphi^2$ scaling, which has long been considered as a key signature of the TPA process, gives way to a radically different, $w_2 \propto \varphi$ behavior of the TPA rate. Much effort has been focused on identifying suitable organic materials that would provide high TPA rates in experiments with entangled photon states [28–33].

An important question that arises in the context of life-science applications is whether or not the enhanced TPA rates attainable for entangled photons can help resolve one of the most pressing problems of nonlinear-optical bioimaging [34–38] — prevent unwanted photochemical and photobiological processes [39–41] by providing a reliably detectable TPA-induced fluorescence at lower levels of laser intensity than those needed for TPA imaging with classical light. Here, we address this and related questions regarding the benefits and limitations of using entangled photon states for multiphoton bioimaging. We show that new approaches in nonlinear and quantum optics, combined with the latest achievements in biotechnologies, open the routes toward efficient photon-entanglement-based strategies in TPA microscopy that can help confront long-standing challenges in life-science imaging. Unleashing the full potential of this approach will require, however, high throughputs of virus-construct delivery, high expression efficiencies of genetically encodable fluorescent markers, high-brightness sources of entangled photons, as well as a thoughtful entanglement engineering in time, space, pulse, and polarization modes. We demonstrate that suitably tailored nonlinear optical fibers can deliver entangled photon pairs confined to entanglement volumes many orders of magnitude smaller than the entanglement volumes attainable through spontaneous parametric down-conversion. These ultracompact modes of entangled photons are shown to enable a radical enhancement of two-photon absorption of entangled photons, opening new avenues for quantum entanglement in life-science imaging.

Three quarters of a century ago, Erwin Schrödinger, one of the founders of quantum physics, as his highly praised attempt to rethink the limits of the possible, has published a book with one of the quintessential eternal questions — "What is Life?" — as its title [42]. Almost six decades later, pioneers of multiphoton microscopy have offered their perspective on early-era TPA bioimaging studies in the form of a review "Nonlinear magic: multiphoton microscopy in the

biosciences" [35]. The latest impressive progress and ground-breaking discoveries in quantum optics, nonlinear microscopy, and optogenetics raise a new question: is quantum magic possible? Can quantum states of light make a difference by providing practically significant benefits for bioimaging? These questions will be the focus of what will follow.

2. Multiphoton life-science imaging with entangled photons: a viable strategy?

2.1 Two-photon absorption of uncorrelated photons
Nonlinear absorption of light is one of only a few nonlinear-optical effects whose various manifestations have been observed experimentally [43–46] and described theoretically [47] long before the advent of the laser. A standard, perturbation-theory approach treats weak-field TPA as a two-step process (Fig. 1a–c) in which absorption of one photon of frequency ω_1 at a moment of time t_1 is followed by absorption of the second photon of frequency ω_2 at time $t_1 + \Delta\tau$. The first step of this process is accomplished via one-photon-allowed virtual transitions of the quantum system from the initial state g to a manifold of intermediate quantum states s (Fig. 1a, c). In the second step, the TPA process is completed through one-photon-allowed virtual transitions coupling intermediate states s to the final state f (Fig. 1a, c). In this textbook TPA picture, the rates of both g → s and s → f transitions are proportional to the field intensity. In the case of frequency-degenerate TPA, $\omega_1 = \omega_2 = \omega$, this gives rise to a signature $R_2 = \sigma_2 \varphi^2$ behavior of the TPA rate as a function of the incident photon flux density φ, with the TPA cross section σ_2 given by [47, 48]

$$\sigma_2(\omega) \propto \left| \sum_s \frac{\mu_{\mathrm{fs}}\,\mu_{\mathrm{sg}}}{\hbar(\omega_{\mathrm{sg}} - \omega)} \right|^2 \rho_{\mathrm{f}}(2\omega),\qquad (1)$$

where μ_{fs} and μ_{sg} are the dipole moments of the s → f and g → s transitions, $\omega_{\mathrm{sg}} = (\varepsilon_s - \varepsilon_g)/\hbar$, ε_s and ε_g are the energy eigenvalues of the s and g states, and $\rho_{\mathrm{f}}(2\omega)$ is the density of states within the band accessed via the g → f TPA process.

For strongly asymmetric molecules, effects related to a permanent dipole moment may become noticeable. For such systems, the sum over states in Eqn (1) should be augmented [48–52] by another, $\sigma_\Delta \propto |\Delta\mu_{\mathrm{fg}}\,\mu_{\mathrm{fg}}|^2$ term, where μ_{fg} is the dipole moment of the g → f ground-to-final-state transition (Fig. 1c), $\Delta\mu_{\mathrm{fg}} = \mu_{\mathrm{f}} - \mu_{\mathrm{g}}$, and μ_{g} and μ_{f} being the ground- and
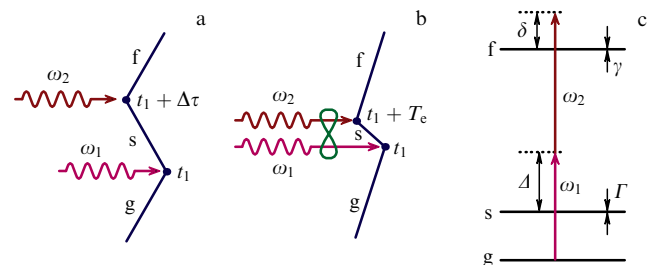
Figure 1. Feynman diagrams (a, b) and an energy-level diagram (c) of a two-photon absorption of uncorrelated (a) and entangled (b, c) photons: g, s, f — initial, intermediate, and final states; Δ — frequency detuning of ω_1 from a one-photon resonance with the g−s transition; δ — frequency detuning of $\omega_1 + \omega_2$ from a two-photon resonance with the g−f transition; Γ, γ — linewidths of the s and f states.

final-state permanent dipole moments of a molecule. The σ_Δ term describes an additional quantum pathway of TPA excitation whereby a pair of entangled or uncorrelated photons can transfer a molecule from its ground state to a real, TPA-allowed state f. This TPA pathway can be represented as a sum of two Feynman diagrams. In one of these diagrams, the system evolves from state g to state f, as it is shown in Fig. 1a for uncorrelated photons and Fig. 1b for entangled photons, but with state s at the intermediate state replaced by state f. In the second diagram, the system evolves from state f to state g, as it is shown in Figs 1a and 1b once again, but with s this time replaced by g. The term represented by the second diagram is shifted in phase by π relative to the term described by the first diagram.

Quantum interference of the two TPA pathways represented by $|\mu_{fs}\,\mu_{sg}|^2$ and $|\Delta\mu_{fg}\,\mu_{fg}|^2$ terms in the TPA cross section suggests interesting options for extending the ideas of quantum control to the TPA of both classical and quantum light [28–33]. As one practically important example, new red-shifted fluorescent proteins can be designed by tuning the $\Delta\mu_{fg}$ permanent-dipole-moment difference via suitable molecular-structure tailoring [53–62], thus providing powerful tools for deep-tissue microscopy, including, but not limited to in vivo deep-brain imaging.

2.2 Two-photon absorption of entangled photons
The situation is drastically different when photons ω_1 and ω_2 exhibit correlations, e.g., quantum entanglement, within time T_e and area A_e. If one of such photons is detected at a position **r** at an instant of time t, then its twin, at the same instant of time, is within a volume $V_e = cA_eT_e$ around **r**, where c is the speed of light. Thus, if one of these photons is absorbed via a g $\to$ s transition at the moment of time t_1, its twin has to complete the TPA process, via the s $\to$ f pathway (Fig. 1b), within a time interval T_e. The rate of such a process is linear in φ, $R_e = \sigma_e\varphi$. The cross section of entangled-pair two-photon absorption (ETPA) can often be estimated as [23, 25]

$$\sigma_e \approx \frac{\sigma_2}{A_e T_e}\,. \tag{2}$$

The TPA total rate is then found as a sum of terms describing the TPA of correlated and uncorrelated photons,

$$R = \sigma_e\varphi + \sigma_2\varphi^2\,. \tag{3}$$

It is straightforward to see from Eqn (3) that the TPA rate is dominated by the conventional, φ^2 term unless $\varphi < \varphi_c \approx \sigma_e/\sigma_2 \approx (A_eT_e)^{-1}$. When cast in the form $\varphi A_e T_e < 1$, this condition shows that the ETPA rate can exceed the TPA rate for uncorrelated photons only when the incident photon flux is so low that there is no more than one photon in this flux per entanglement area A_e per entanglement time T_e.

This result is in no way surprising. Indeed, the $\sigma_e\varphi$ term in the TPA rate can only be comparable to or larger than the conventional, $\sigma_2\varphi^2$ TPA term only when the photon flux density is too low for the $\sigma_2\varphi^2$ TPA part to build up. In other words, the photon flux density should be so low that each molecule simply does not see the second uncorrelated photon within the entanglement area and within the entanglement time. For bioimaging, with its continuing desperate struggle to provide more laser photons per molecule for a more intense fluorescence signal, the $\varphi A_e T_e < 1$ requirement may seem to be simply too much to bear, ruling out even a thinnest chance for success. Fortunately, unique properties of entangled

photon states, including, above all, the strong confinement of these states to the V_e volume, provide powerful resources to turn the tide.

2.3 Fluorescence count rates
To provide insights into how entangled photon states could help confront long-standing challenges in multiphoton bioimaging, we proceed with a semi-quantitative analysis of photon count rates attainable in a fully quantum, ETPA modality of fluorescence imaging. For an incident photon flux density $\varphi \approx \varphi_c$, an order-of-magnitude estimate for the TPA rate as defined by Eqn (3) gives

$$R_c \approx \sigma_2(A_e T_e)^{-2}\,. \tag{4}$$

We consider a typical nonlinear bioimaging setting (Fig. 2) in which a laser beam illuminates a targeted cell, inducing a fluorescent response from a TPA-excited fluorescent marker whose expression in the cell is encoded by a genetic sequence delivered to the cell with a suitable virus construct. Assuming that the laser beam area is A_e, we find that the number of fluorescence photons detected in such a setting per unit time is

$$n_{ph} \approx \frac{\zeta\vartheta}{A_e T_e^2}\,\eta\sigma_2\,, \tag{5}$$

where η is the quantum yield of the fluorescent marker, ζ is the fluorescence collection efficiency, and ϑ is the surface density of fluorescent marker molecules on the cell membrane.

2.4 Understanding TPA cross sections
Combined with the Feynman diagram of the TPA process in Fig. 1a, Eqn (1) suggests a useful order-of-magnitude estimate for the TPA cross section:

$$\sigma_2 \approx S^2\Delta\tau\,. \tag{6}$$

where $S \sim d^2$ is the effective cross-sectional area, d is the dipole length of a molecule, and $\Delta\tau$ is a fictitious virtual-state lifetime (Fig. 1c).

Equation (6) offers helpful insights into the physics behind the TPA of entangled photons. Indeed, combining Eqns (2)
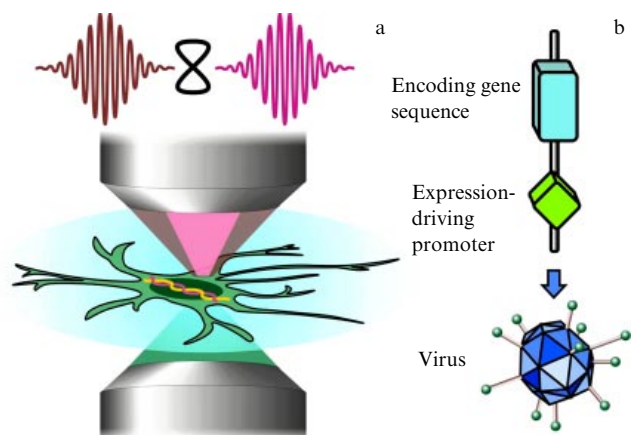

Figure 2. Typical optogenetics-enabled nonlinear bioimaging setting: a laser beam is focused by the upper microscope objective to illuminate a cell, inducing an optical response from a TPA-excited fluorescent marker whose expression in the cell is encoded by a genetic sequence delivered to the cell with a suitable virus construct, as shown on the right.

and (6), we find $\sigma_e = p_s p_t S$, where $p_s = S/A_e$ and $p_t = \Delta\tau/T_e$. Since $S \ll A_e$ and $\Delta\tau \ll T_e$ for any conceivable setting of TPA imaging, the ETPA cross section can be viewed as a product of the cross section of one-photon absorption, $\sigma_1 \propto S$, and the probabilities $p_t = \Delta\tau/T_e \ll 1$ and $p_s = S/A_e \ll 1$ of finding the entangled photons within the virtual-state lifetime $\Delta\tau$ and within the area of a molecule S. This view is consistent with a notion of ETPA as a process in which one-photon absorption of the first photon from an entangled photon pair (photon ω_1 in Fig. 1b) is promptly followed by the absorption of the twin photon (photon ω_2 in Fig. 1b). That the ETPA cross section is factorized into a product of S and $P_V = p_t p_s$ thus merely reflects the fact that, each time when the first photon is absorbed by a molecule (with the probability of this event proportional to S), the second photon is always absorbed whenever it is found (with a probability $P_V = p_t p_s$) within a confinement volume $V_e = cS\Delta\tau$.

2.5 TPA cross sections in nonlinear bioimaging
In nonlinear bioimaging, the laser frequency ω is chosen in such a way as to avoid one-photon resonances in order to prevent a strong attenuation of the pump and reduce the heating of a biotissue. In this regime, all the frequency denominators in Eqn (1) are much larger than the relevant linewidths $\Gamma_s, |\omega_{sg} - \omega| \gg \Gamma_s \sim \Gamma$ (Fig. 1c). It is straightforward to see from Eqn (1) that the virtual-state lifetime $\Delta\tau$ then relates to the frequency detuning $\Delta\omega = |\omega_{sg} - \omega|$ of the g $\to$ s transition dominating the sum over states (SOS) in Eqn (1), $\Delta\tau \sim 1/\Delta\omega$. With the most natural set of parameters, $d \approx 10^{-8} - 10^{-9}$ cm, $S \approx 10^{-16} - 10^{-17}$ cm^2, and $\Delta\tau \approx 0.1 - 1$ fs, Eqn (1) leads to $\sigma_2 \approx 1 - 1000$ GM (1 GM = 10^{-50} cm^4 s/photon), providing, with specific values of d and $\Delta\tau$, a reasonable order-of magnitude estimate for the TPA cross sections for a vast and rich palette of fluorophores used in nonlinear bioimaging [63].

2.6 Polarization dependence of the TPA cross section
Much care needs to be exercised, however, in extending these estimates to a TPA of entangled photons. One possible source of difficulties of such an extension is the polarization dependence of the TPA cross section. Powerful in its simplicity, Eqn (6) offers important insights into the fundamental physical factors defining TPA cross sections and provides a helpful order-of-magnitude estimate for the σ_2 values of a remarkably broad range of molecular systems. The estimate of Eqn (6), however, is based on an implicit assumption that the two laser photons involved in the TPA process (Fig. 1a–c) share the same polarization. Most natural in the context of TPA imaging, this assumption is not always justified for ETPA settings. Specifically, in one of the most widely spread schemes of photon-entanglement generation, based on spontaneous parametric down conversion (SPDC) in nonlinear crystals, entangled photons generated as a part of the photon-pair SPDC output are, in fact, cross-polarized. The TPA cross section for such a polarization geometry, $\sigma_{2\perp}$, can easily be an order of magnitude smaller than the TPA cross section, $\sigma_{2\parallel}$, probed by two copolarized fields [64, 65].

2.7 Biotechnology factors: virus-construct delivery and fluorescent marker expression
On the biotechnology side, Eqn (5) leads us to appreciate the significance of the efficiency of virus-construct delivery and fluorescent marker expression [66–68] in a targeted cell in optical bioimaging (see Fig. 2). A higher efficiency of fluorophore expression will translate into a higher surface density ϑ of fluorescent marker molecules on a cell membrane (Fig. 2), leading to a more intense fluorescence signal. The specific values of ϑ may widely vary, depending on the type of fluorescent marker, genetic sequence chosen to encode this marker, virus construct, and virus delivery method [69, 70]. For our analysis here, we set our estimate of this parameter at the level of $\vartheta \approx 10^4$ μm^{-2}, corresponding to the highest efficiencies of virus-construct delivery and highest fluorescent-marker expression efficiencies attainable with cutting-edge optogenetic technologies [71].

2.8 Entanglement area and entanglement time
With spontaneous parametric down conversion used as a source of entangled photon states, a typical entanglement time is $T_e \approx 100$ fs. The spatial mode structure of the entangled-photon SPDC output can be quite complex [72] and far from a high-purity entangled state. The entanglement area can broadly vary for such a source of photon entanglement, depending on the dispersion of the crystal and the properties of the laser pump field. This gives rise to a broad range of A_e values, sometimes as different as $A_e \approx 1000$ μm^2 [25] and $A_e \approx 4$ cm^2 [33]. In our analysis below, we base our estimate of the entanglement area on a typical beam size of a photon-pair SPDC output, $d_e \sim 1$ mm, leading to $A_e \approx 10^{-2}$ cm^2.

2.9 Quantifying the fluorescence readout in entangled-photon TPA bioimaging: where we are now and where to head
We can now proceed with an estimate for the fluorescence photon count rate n_{ph} in a typical nonlinear bioimaging setting with an SPDC source of entangled photon states. Aiming at an optimistic, yet realistic estimate for nph, we take the quantum yield $\eta \approx 1$, the fluorescence collection efficiency $\zeta \approx 0.1$, entanglement time $T_e \approx 100$ fs, entanglement area $A_e \approx 10^{-2}$ cm^2, and the surface density of fluorescent marker molecules on the cell membrane $\vartheta \approx 10^4$ μm^{-2}. The fluorescence photon count rate is then estimated as $n_{ph} \approx 10^{-7}$ photons s^{-1} with $\sigma_{2\parallel} \approx 1000$ GM taken for copolarized fields and $n_{ph} \approx 10^{-8}$ photons s^{-1} with $\sigma_{2\perp} \approx 100$ GM for cross-polarized photons. These levels of n_{ph} are clearly several orders of magnitude lower than the dark count rate of the most sensitive photon counters.

As discouraging as it may seem, this result, as we will show below, still leaves some much-needed room for maneuver. We are going to show that even with such severe limitations on n_{ph}, entangled photons can still be beneficial for multiphoton bioimaging. Securing these benefits, however, requires a suitable high-brightness source of low-A_e, short-T_e photon entanglement. Below, we examine viable options for such a bioimaging setting.

3. Nonlinear fiber optics as a platform for photon entanglement engineering

3.1 Entangled photons from optical fibers
Spontaneous parametric down-conversion in a quadratically nonlinear crystal provides a versatile source of entangled photon pairs (Fig. 3a) for a vast range of quantum-optic studies. In our search for a suitable source of entanglement for multiphoton bioimaging, however, we have to fulfill very
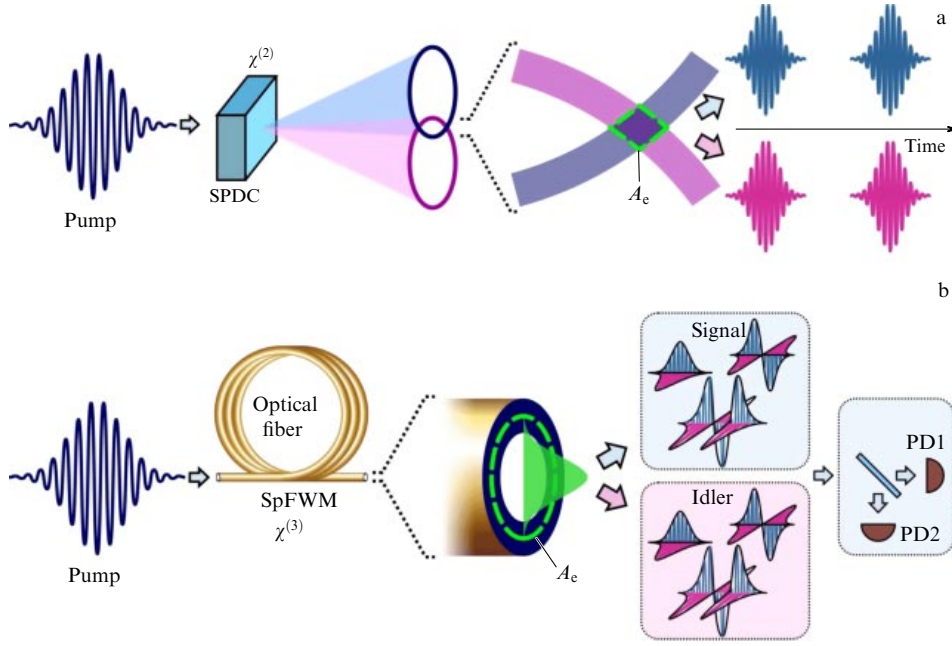
Figure 3. Generation of entangled photon pairs via spontaneous parametric down conversion (SPDC) in a nonlinear crystal (a) and spontaneous four-wave mixing (SpFWM) in an optical fiber (b). Also shown are the pulse modes of the signal and idler entangled photon wave packets at the output of the fiber source of photon entanglement; $\chi^{(2)}$ and $\chi^{(3)}$ are the second and third-order nonlinear-optical susceptibilities.

specific requirements of high brightness provided within a compact entanglement volume. This set of requirements leads us to explore what FWM in an optical fiber has to offer as a source of entangled photon pairs for multiphoton bioimaging. We will show that spontaneous FWM in optical fibers [73–81] provides a vast arsenal of methods and an ample parameter space for photon entanglement engineering in spectral, temporal, spatial and polarization modes (Fig. 3b).

With suitable field-profile tailoring, which can be performed via high-precision fiber structure engineering [82–84], the entangled-photon FWM fiber output can be tightly confined [85–88] within small-A_e waveguide modes (Fig. 3b). Advanced methods of fiber dispersion management [89], on the other hand, may prove instrumental for entanglement-time engineering. Finally, with the available fiber-birefringence tailoring technologies [89–93], phase matching for the entire manifold of FWM polarization modes can be provided [94], with the entangled FWM sidebands generated either in parallel- or cross-polarized modes, thus enabling TPA polarization optimization.

The photon-pair output of such an FWM process is an entangled broadband state ket, whose description generally requires a multidimensional Hilbert space. In a standard perturbative treatment, this two-photon state is given by [95]

$$|\Psi\rangle = \kappa \iint F(\omega_1, \omega_2)\, \hat{a}_{j1}^\dagger(\omega_1)\, \hat{a}_{j2}^\dagger(\omega_2)|0\rangle_{j1}|0\rangle_{j2}\, d\omega_1\, d\omega_2\,, \quad (7)$$

where κ is the optical gain, $F(\omega_1, \omega_2)$ is the joint spectral amplitude (JSA) function, $\hat{a}_{j1}^\dagger(\omega)$ and $\hat{a}_{j2}^\dagger(\omega)$ are the creation operators for photons with a central frequency ω in polarization modes j_1 and j_2, respectively.

In the general case, the JSA function is not factorizable as a product of functions of ω_1 and ω_2. For $\omega_{p1} + \omega_{p2} = \omega_s + \omega_i$ FWM driven by pump fields with spectral amplitudes $\alpha_1(\omega)$

and $\alpha_2(\omega)$, the JSA function is given by [95]

$$F(\omega_s, \omega_i) = \int \alpha_1(\omega')\,\alpha_2(\omega_s + \omega_i - \omega')\,\Phi(\omega', \omega_s, \omega_i)\, d\omega'\,, \quad (8)$$

where

$$\Phi(\omega', \omega_s, \omega_i) = \mathrm{sinc}\left[\Delta\beta(\omega', \omega_s, \omega_i)\frac{L}{2}\right]$$
$$\times \exp\left[i\Delta\beta(\omega', \omega_s, \omega_i)\frac{L}{2}\right] \quad (9)$$

is the phase-matching function, L is the length of the nonlinear medium and

$$\Delta\beta(\omega', \omega_s, \omega_i) = \beta(\omega') + \beta(\omega_s + \omega_i - \omega')$$
$$- \beta(\omega_s) - \beta(\omega_i) - (\gamma_1 P_1 + \gamma_2 P_2) \quad (10)$$

is the mismatch of the frequency-dependent propagation constants $\beta(\omega)$ of the fields involved in the FWM process, γ_1 and γ_2 are the relevant nonlinear coefficient and P_1 and P_2 are the peak powers of the pump fields.

3.2 Entanglement-time engineering
As can be seen from Eqns (7)–(10), the useful bandwidth of an entangled photon pair and, hence, the entanglement time T_e are controlled by the phase and group-velocity mismatch. For certain settings, the entanglement time Te is defined as the group delay τ_g of the photons in the pair [26–33]. Even though this simple relation between T_e and τ_g is not universal, the significance of the phase mismatch and the group delay as the key parameters defining T_e is invariable. As an invaluable resource for T_e engineering, the phase mismatch and group delay in fiber-optic FWM can be fine-adjusted by choosing a fiber with a suitable dispersion profile and by launching the pump fields into best-suited spatial, temporal, and polarization modes (Figs 3b, 4a, b).

In Figs 4a–f, we illustrate these arguments by presenting phase-matching maps and showing the behavior of the group delay τ_g as a function of the driver wavelength for two different polarization geometries of FWM (Fig. 4a, b) in a fused silica photonic-crystal fiber with a core radius of 1.4 μm and the air-filling fraction of the cladding $f = 0.32$ (see the inset in Fig. 5a). The profile of the group-velocity dispersion (GVD) of this fiber is presented in Fig. 5b. As can be seen from these calculations, a remarkably broadband phase matching can be achieved for the $\omega_{p1} + \omega_{p2} = \omega_s + \omega_i$ FWM process in the ss−ff polarization geometry, where the two pump fields are polarized along the slow (s) fiber axis, while the signal and the idler fields are both polarized along the fast (f) fiber axis. Within the phase-matching region, the group velocities of the signal and idler pulses are close to each other. In this setting the entanglement time can be tuned from less than a femtosecond up to several picoseconds by varying the fiber length. These results show how advantageous the fiber-format FWM is as a source of entangled photon pairs with a tunable entanglement time.

3.3 The mode structure of entangled-photon states
A broad bandwidth of entangled photon packets (1) that generated in nonlinear optical fiber driven by ultrashort laser pulses suggests that temporal mode engineering may add a powerful resource to help tailor photon entanglement for the purposes of multiphoton bioimaging. To understand the mode structure of the continuous-variable entanglement of the two-photon state $|\Psi\rangle$ as defined by Eqns (7)–(10), it is instructive to resort to the Schmidt decomposition of the JSA function [96],

$$F(\omega_1, \omega_2) = \sum_n \sqrt{\lambda_n}\, \psi_n(\omega_1)\, \varphi_n(\omega_2)\,. \qquad (11)$$

Here, λ_n, $\psi_n(\omega)$, and $\varphi_n(\omega)$ are found as the eigenvalues and eigenfunctions of the integral equations

$$\int K_1(\omega, \omega')\,\psi_n(\omega')\,\mathrm{d}\omega' = \lambda_n \psi_n(\omega)\,, \qquad (12)$$

$$\int K_2(\omega, \omega')\,\varphi_n(\omega')\,\mathrm{d}\omega' = \lambda_n \varphi_n(\omega)\,, \qquad (13)$$

where

$$K_1(\omega, \omega') = \int F(\omega, \omega'')\, F^*(\omega', \omega'')\,\mathrm{d}\omega''\,,$$

$$K_2(\omega, \omega') = \int F(\omega'', \omega)\, F^*(\omega'', \omega')\,\mathrm{d}\omega''\,.$$

Introducing the effective creation operators,

$$\hat{b}_n^\dagger = \int \psi_n(\omega_1)\, \hat{a}_{j1}^\dagger(\omega_1)\,\mathrm{d}\omega_1\,, \qquad (14)$$

$$\hat{c}_n^\dagger = \int \varphi_n(\omega_2)\, \hat{a}_{j2}^\dagger(\omega_2)\,\mathrm{d}\omega_2\,, \qquad (15)$$

we can represent the two-photon state $|\Psi\rangle$ as

$$|\Psi\rangle = \sum_n \sqrt{\lambda_n}\, \hat{b}_n^\dagger \hat{c}_n^\dagger |0\rangle_{j1} |0\rangle_{j2}\,. \qquad (16)$$

With the λ_n coefficients found from Eqns (12) and (13), we can quantify the entanglement in terms of the entropy [80], $S = -\sum_n \lambda_n \log_2 \lambda_n$. The Schmidt parameter, defined as $K = 1/\sum_n \lambda_n^2$, provides a measure for the dimensionality of the Hilbert space (or the number of biphoton modes) needed to describe the entanglement [97], with the purity of the two-photon state quantified as $p = 1/K$.

As an instructive example of fiber-based entanglement engineering, Fig. 4g, h presents the JSA functions and the Schmidt eigenvalues calculated for a photon-pair FWM output of a fiber with the above-specified parameters driven by two cross-polarized pump fields, giving rise to the signal and idler fields detected in the s and f polarization modes, respectively. This polarization geometry is referred to as sf−fs hereinafter. With the central wavelength of the pump set at $\lambda_p = 800$ nm, the central maximum of the phase-matching function $\Phi(\omega', \omega_s, \omega_i)$ for this FWM process gives rise to an almost horizontal stripe at the center of the JSA map (Fig. 4g), representing $\approx 98\%$ of the photon-pair generation probability. If only the entire signal bandwidth, $\Delta\omega_s \approx 35$ THz, within this central lobe of the JSA map could be accommodated by a single spectral mode $\psi_1(\omega)$, the photon-pair output would be overwhelmingly dominated by biphotons with a factorizable wave function $|\Psi\rangle$.

Results of the Schmidt-mode analysis, presented in Fig. 4h, show that the structure of the central lobe in the JSA map in Fig. 4g can indeed be accurately approximated as a product of two spectral modes $\psi_1(\omega)$ and $\varphi_1(\omega)$. This pair of modes enters into the Schmidt decomposition of Eqn (11) with a weighting factor $\sqrt{\lambda_1} \approx 0.99$, thus accounting for 99% of the two-photon state generated as the fiber output. The second largest λ_n coefficient in this expansion is almost two orders of magnitude smaller than λ_2 (Fig. 4h). The purity of the photon-pair FWM output in this regime is $p \approx 0.96$. The entanglement entropy is $S \approx 0.15$ (Fig. 4h). The effective dimensionality of the Hilbert space needed to describe the entanglement structure of such a two-photon state is $K \approx 1.04$.

It is remarkable that, with a rather simple fiber design, vectorial FWM can be steered toward high-purity photon-pair generation with a pump at around 800 nm — the central wavelength of Ti: sapphire short-pulse laser sources. Off this wavelength, the sf−fs FWM tends to deliver two-photon states whose continuous-variable spectral entanglement structure can only be described in a Hilbert space of higher dimensionality.

3.4 Entanglement-area engineering
In this section, we will show that the fiber format of photon-pair generation offers unique solutions for entanglement area engineering. To this end, we consider a generic waveguide structure with an arbitrary transverse profile of the refractive index $n(r)$. The field of the waveguide mode supported by such a structure is written as [98]

$$E(r, \varphi, z, t) = F(r) \cos(m\varphi) \exp(-\mathrm{i}\beta z) \exp(\mathrm{i}\omega t)\,, \qquad (17)$$

where z, r, and φ are the cylindrical coordinates, t is the time, $F(r)$ is the transverse field profile in the waveguide mode, m is the azimuthal mode index, β is the propagation constant, and ω is the radiation frequency.

The transverse field profile in the waveguide mode can be found by solving the relevant wave equation:

$$\frac{\mathrm{d}^2 F}{\mathrm{d}r^2} + \frac{1}{r}\frac{\mathrm{d}F}{\mathrm{d}r} + \left\{ \left[\frac{\omega}{c}\, n(r) \right]^2 - \beta^2 - \frac{m^2}{r^2} \right\} F = 0\,. \qquad (18)$$
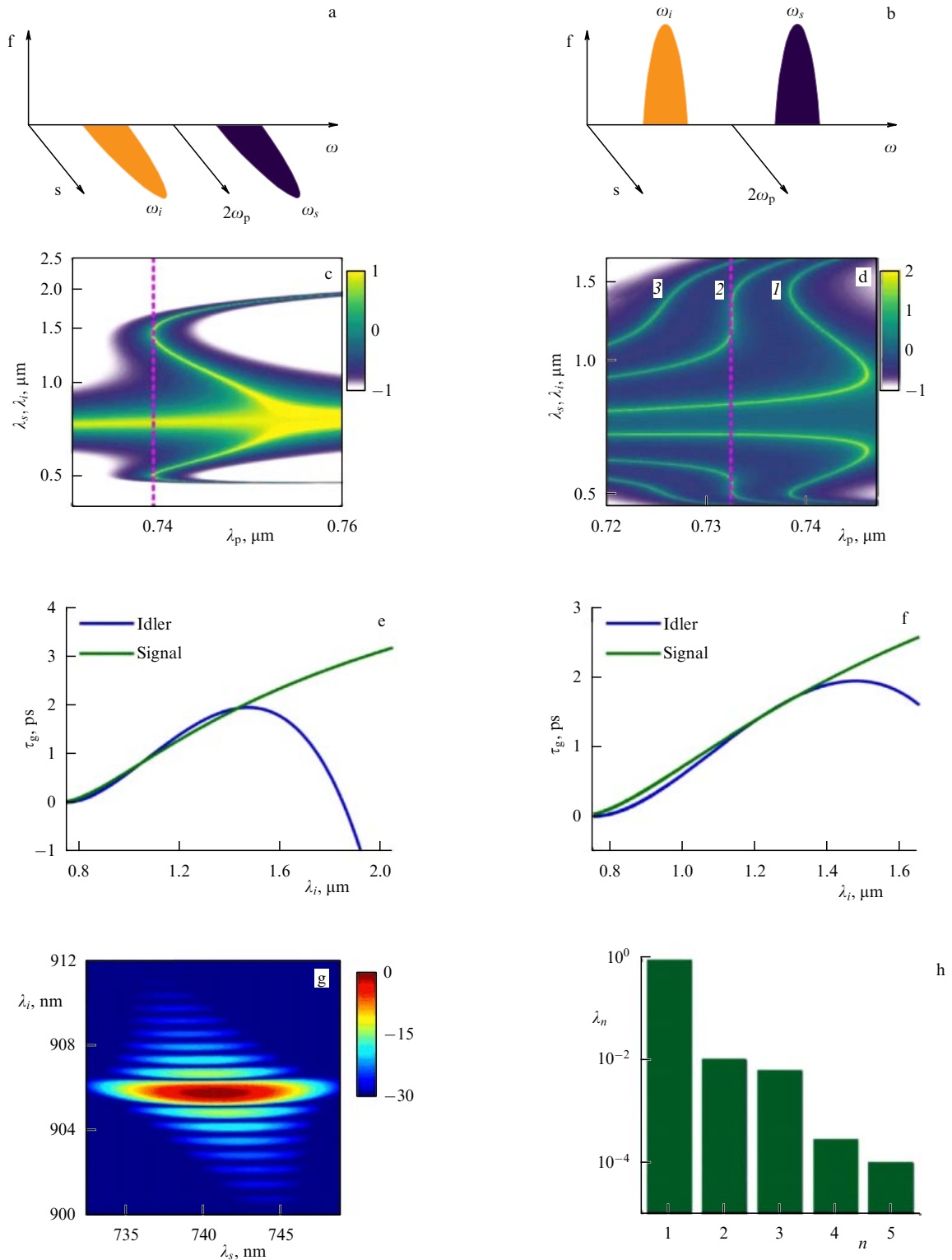
Figure 4. (a, b) Polarization geometries in $2\omega_p = \omega_s + \omega_i$ four-wave mixing in a birefringent optical fiber with fast and slow axes f and s and (c, d) the respective phase-matching maps, showing the coherence length $l_c = \pi/|\Delta\beta|$ as a function of the pump, signal, and idler wavelengths. (e, f) The group delay of the idler and signal photon wave packets at the output of a 5-cm-long stretch of a fiber. (g) The joint spectral amplitude $F(\lambda_s, \lambda_i)$ and (h) the eigenvalues λ_n for a two-photon state generated through the sf–fs polarization geometry of $2\omega_p = \omega_s + \omega_i$ four-wave mixing with a pump at $\lambda_p = 800$ nm. Calculations are performed for four-wave mixing in a photonic-crystal fiber with a core radius $a = 1.44$ μm, an air-filling fraction $f = 0.32$, the nonlinearity coefficient $\gamma = 100$ W^{-1} km^{-1}, and a birefringence $\delta n = 0$ (c), $\delta n = 10^{-5}$ (d, curve *1*), $\delta n = 0.98 \times 10^{-4}$ (d, curve *2*), and $\delta n = 2 \times 10^{-4}$ (d, curve *3*).
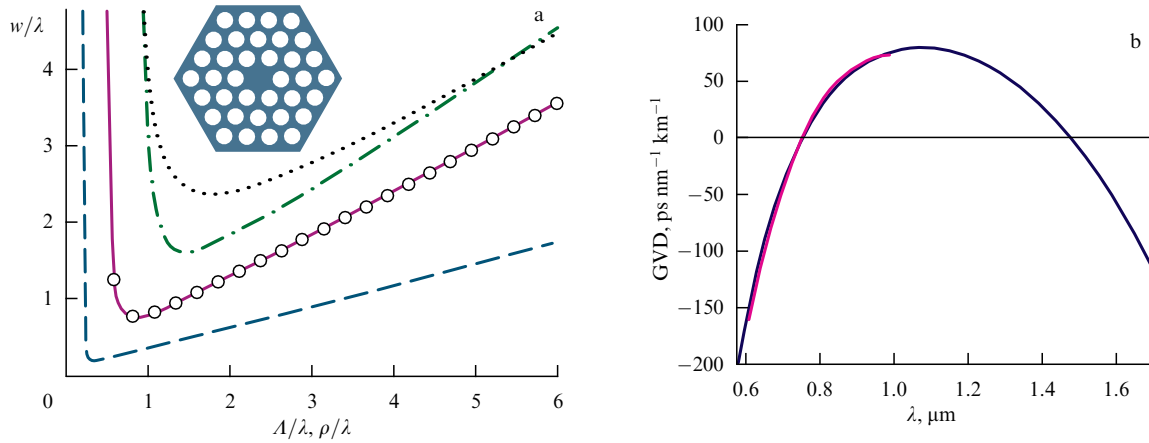
Figure 5. (a) The effective radius of the guided mode in a silica PCF as a function of the lattice constant Λ of the hexagonal fiber cladding calculated by using the approximation of Eqn (25) for $\lambda = 1\ \mu m$, $d/\Lambda = 0.3$ (dash-dotted line), 0.5 (solid line), and 0.9 (dashed line). Numerical solution of Eqn (18) is shown by open circles. The dotted line presents the effective radius of the fundamental mode of a standard fiber with $n_1 - n_2 = 0.01$ as a function of the core size ρ. Photonic-crystal fiber with a hexagonal-lattice cladding is shown in the inset. (b) The profile of the group-velocity dispersion (GVD) of an optical fiber used in calculations.

The effective mode radius is defined as

$$w = \left(\frac{S}{\pi}\right)^{1/2}, \qquad (19)$$

where

$$S = \frac{2\pi\left[\int_0^\infty |F(r)|^2 r\,dr\right]^2}{\int_0^\infty |F(r)|^4 r\,dr} \qquad (20)$$

is the effective mode area.

We represent the transverse profile of the refractive index in the waveguide structure as

$$n(r) = \begin{cases} n_1\left[1 - 2\left(\frac{r}{\rho}\right)^g \Delta\right]^{1/2}, & 0 \leqslant r \leqslant \rho, \\ n_2 = n_1(1 - 2\Delta)^{1/2}, & \rho \leqslant r, \end{cases} \qquad (21)$$

where n_1 and n_2 are the refractive indices of the materials forming the waveguide structure, ρ is the core radius, and $\Delta = (n_1^2 - n_2^2)/(2n_1^2)$. The exponent g in Eqn (21) controls the steepness of the refractive-index profile in the waveguide, with $g = 1$ corresponding to a triangular profile of $n(r)$ and $g = 2$ recovering a parabolic refractive-index profile. With a very large g, Eqn (21) describes a step-index waveguide.

For a standard optical fiber, the mode radius can be quite accurately approximated with the Marcuse formula [99],

$$\frac{w}{\rho} \approx \frac{A}{V^{2/(2+g)}} + \frac{B}{V^{3/2}} + \frac{C}{V^6}, \qquad (22)$$

where

$$V = \frac{2\pi\rho}{\lambda}(n_1^2 - n_2^2)^{1/2} \qquad (23)$$

is the waveguide parameter; λ is the radiation wavelength; and A, B, and C are numerical constants.

For a step-index optical fiber, $g \to \infty$, the numerical constants in Eqn (22) are [99] $A = 0.65$, $B = 1.619$, and $C = 2.879$. The dotted line in Fig. 5a presents the mode radius w normalized to the wavelength λ calculated as a function of the fiber core radius ρ for a standard weakly guiding optical fiber with $n_1 - n_2 = 0.01$.

The waveguide parameter V quantifies the balance between diffraction and confinement of an optical beam due to total internal reflection in a waveguide structure. For a step-index fiber ($g \to \infty$) with large V, the mode radius w, as can be seen from Eqn (22) scales linearly with the core radius (the dotted line in Fig. 5a), $w \approx A\rho$. For lower V, field confinement to the fiber core becomes weaker [87, 98]. As a consequence, for low V, a decrease in ρ leads to the growth in the mode radius (see the dotted line in Fig. 5a).

Let us consider now a waveguide with a cross-section structure typical of a photonic-crystal fiber (PCF) [82] (the inset in Fig. 5a). The central part of this waveguide, which serves as a waveguide core, is surrounded by a cladding that is built on a hexagonal lattice of air holes with a diameter d arranged in a periodic structure with a lattice constant Λ. For a fiber of this type, the waveguide parameter can be defined as [100]

$$V_{PCF} = \frac{2\pi\Lambda}{\lambda}(n_1^2 - n_{eff}^2)^{1/2}, \qquad (24)$$

where n_{eff} is the effective refractive index of the structured cladding, understood as the effective index of the fundamental space-filling mode of an infinite ideal hexagonal lattice of air holes with a diameter d separated by Λ.

With an appropriate choice of numerical constants ($A_{PCF} = 0.7078$, $B_{PCF} = 0.2997$, $C_{PCF} = 0.0037$, $g_{PCF} = 8$), a modified Marcuse formula [100]

$$\frac{w}{\Lambda} \approx \frac{A_{PCF}}{V_{PCF}^{2/(2+g)}} + \frac{B_{PCF}}{V_{PCF}^{3/2}} + \frac{C_{PCF}}{V_{PCF}^6}. \qquad (25)$$

provides an adequate accuracy of approximation of the ratio w/Λ as a function of V_{PCF}. Figure 5a compares calculations for the mode radius as a function of the lattice constant Λ performed [101] with the use of Eqn (25) (solid line) and through a numerical solution of Eqn (18) (open circles). Within the considered range of parameters, predictions of the approximate formula (25) deviate from the results of numerical simulations by less than 2%.

For given d/Λ, the waveguide parameter V_{PCF} provides, similar to the V parameter of a standard fiber, a quantitative measure of the balance between diffraction and waveguide confinement of an optical beam. High V_{PCF} values correspond to a strong field confinement in the fiber core. In this regime, the mode radius increases with the growth in Λ. For low V_{PCF}, a decrease in Λ gradually weakens field confinement in the fiber core. These opposite tendencies give rise to a minimum in the dependence of the mode radius on the lattice constant Λ (Fig. 5a). An increase in d/Λ lowers the effective refractive index n_{eff} of the PCF cladding, thus increasing V_{PCF} for a given value of Λ/λ. When d/Λ is sufficiently small, the PCF can guide only one mode ($V_{PCF} < 2$ for $d/\Lambda = 0.3$). The minimum mode radius is then $w_{min} \approx 1.6\lambda$ (dash-dotted line in Fig. 5a). In the case of large d/Λ, the field is tightly confined to the fiber core even for small Λ/λ. In this regime, the minimum mode radius for $d/\Lambda = 0.9$, $w_{min} \approx 0.22\lambda$, is achieved with $\Lambda \approx 0.37\lambda$ (dashed line in Fig. 5a).

Several technologies are currently available for the fabrication of submicrometer-core waveguides. In fibers fabricated by means of PCF technologies, optical radiation can be guided along glass channels with a radius less than 200 nm [86, 87]. High values of the index contrast Δ, typical of such waveguide systems, provide a strong confinement of the field in the glass channel, enhancing a broad class of nonlinear-optical processes — from self-phase modulation and FWM to multioctave supercontinuum generation [102–105]. Spontaneous FWM in such fibers provides an efficient source of entangled photon pairs. The area A_e within these pairs are generated can be tailored, as the analysis presented in this section shows, from hundreds of nanometers to a few micrometers.

4. Toward life-science imaging with entangled photons

We now have enough ammunition to re-examine the limits of the possible for bioimaging with entangled photons. With all the effort invested within the past decades into engineering high-quantum-yield fluorescent probes and optimizing signal collection in various imaging schemes, there is not much that can be done to further increase η and ζ. We, therefore, keep these parameters at the same level, $\eta \approx 1$ and $\zeta \approx 0.1$.

Impressive progress has been recently achieved in the research aimed at designing high-σ_2 fluorescent markers for multiphoton imaging. It remains to be seen, however, whether the increase in σ_2 in a new generation of fluorescent probes can be efficiently decoupled from a reduction in the surface density ϑ of fluorescent molecules on the cell membrane since higher TPA cross sections are often achieved by increasing the number of fluorophore units in a molecule, which inevitably yields molecules with a larger size and volume. Yet, it is not unreasonable to take $\sigma_2 \approx 10^4$ GM for a realistic estimate.

Enhancing the efficiency of fluorescent marker expression in a targeted cell remains a focus of extensive research, with a strong motivation provided by the progress in optogenetics [66–68] and, since recently, thermogenetics [106–111]. With all the recent achievements in this rapidly growing area of biotechnologies [112], an on-membrane fluorescent-probe surface density $\vartheta \approx 10^5$ μm^{-2} is within reach.

Achieving higher σ_2 and ϑ is difficult as it involves complex molecule design and encounters fundamental limitations, some of which are still to be adequatelyunderstood. Equations (1) and (6) provide much-needed physical insights

into the factors limiting the TPA cross sections in a bioimaging setting. As can be seen from these formulas, options for TPA enhancement are largely limited to an increase in sizes of a molecule or searching for suitable intermediate states that could reduce the frequency denominators $\Delta\omega$. However, larger sizes of molecules will almost inevitably lead to lower surface densities ϑ of these molecules on the cell membrane, while smaller $\Delta\omega$ will enhance one-photon absorption — a big no-no in life-science imaging. An order-of-magnitude increase in σ_2 and ϑ is, perhaps, the best we can hope for within the next few years. It is with these thoughts in mind that we limit our wishful thinking to $\sigma_2 \approx 10^4$ GM and $\vartheta \approx 10^5$ μm^{-2} in our further analysis.

Entanglement-time and entanglement-area engineering, on the other hand, promises much faster and much more significant returns. With a photon entanglement output of a suitably tailored fiber-optic source confined within an entanglement time $T_e \approx 1$ fs and entanglement area $A_e \approx 10^{-8}$ cm^2, the fluorescence photon count rate nph can be increased, in accordance with Eqn (5), by 10 orders of magnitude compared to n_{ph} in ETPA imaging performed with a standard, $T_e \approx 100$ fs, $A_e \approx 10^{-2}$ cm^2 SPDC source of entangled photons.

When combined with $\sigma_2 \approx 10^4$ GM and $\vartheta \approx 10^5$ μm^{-2}, this leads to a fluorescence photon count rate $n_{ph} \approx 10^5$ photons s^{-1}, providing a comfortable level of signal read-out, well above the dark count rate of standard photon counters used in quantum optics and even laser microscopy. Suitably engineered arrays of fiber-optic sources of entangled photons can help further boost the ETPA-induced fluorescence signal and push n_{ph} to the level sufficient for video-rate imaging.

5. Conclusion

To summarize, we have shown that that new approaches in nonlinear and quantum optics, combined with the latest achievements in biotechnologies, open the routes toward efficient photon-entanglement-based strategies in MPA microscopy that can help confront long-standing challenges in life-science imaging. Unleashing the full potential of this approach requires high throughputs of virus-construct delivery, high expression efficiencies of genetically encodable fluorescent markers, high-brightness sources of entangled photons, as well as a thoughtful entanglement engineering in time, space, pulse, and polarization modes. We have demonstrated that suitably tailored nonlinear optical fibers can deliver entangled photon pairs confined to entanglement volumes many orders of magnitude smaller than the entanglement volumes attainable through spontaneous parametric down-conversion. These ultracompact modes of entangled photons have been shown to enable a radical enhancement of two-photon absorption of entangled photons, opening new avenues for quantum entanglement in life-science imaging. Is quantum magic in life-science imaging possible? We will know soon.

References

1. Gisin N, Thew R *Nat. Photon.* **1** 165 (2007)
2. Giovannetti V, Lloyd S, Maccone L *Nat. Photon.* **5** 222 (2011)
3. Liao S-K et al. *Nature* **549** 43 (2017)
4. Ma X-S et al. *Nature* **489** 269 (2012)
5. Kim Y-H et al. *Phys. Rev. Lett.* **84** 1 (2000)
6. Ren J-G et al. *Nature* **549** 70 (2017)
7. Qiang X et al. *Nat. Photon.* **12** 534 (2018)
8. Taylor M A, Bowen W P *Phys. Rep.* **615** 1 (2016)
9. Tegmark M *Phys. Rev. E* **61** 4194 (2000)
10. Boyer V et al. *Science* **321** 544 (2008)
11. Lloyd S *Science* **321** 1463 (2008)
12. Shapiro J H, Lloyd S *New J. Phys.* **11** 063045 (2009)
13. Brida G, Genovese M, Berchera I R *Nat. Photon.* **4** 227 (2010)
14. Ono T, Okamoto R, Takeuchi S *Nat. Commun.* **4** 2426 (2013)
15. Lemos G B et al. *Nature* **512** 409 (2014)
16. Gariepy G et al. *Nat. Commun.* **6** 6021 (2015)
17. Classen A et al. *Optica* **4** 580 (2017)
18. Moreau P-A et al. *Nat. Rev. Phys.* **1** 367 (2019)
19. Tenne R et al. *Nat. Photon.* **13** 116 (2019)
20. Toninelli E et al. *Optica* **6** 347 (2019)
21. Nagasako E M et al. *Phys. Rev. A* **64** 043802 (2001)
22. Liao Z, Al-Amri M, Zubairy M S *Phys. Rev. Lett.* **105** 183601 (2010)
23. Javanainen J, Gould P L *Phys. Rev. A* **41** 5088 (1990)
24. Gea-Banacloche J *Phys. Rev. Lett.* **62** 1603 (1989)
25. Fei H-B et al. *Phys. Rev. Lett.* **78** 1679 (1997)
26. Saleh B E A et al. *Phys. Rev. Lett.* **80** 3483 (1998)
27. Maleki Y, Zheltikov A M *Sci. Rep.* **9** 16780 (2019)
28. Lee D-I, Goodson T *J. Phys. Chem. B* **110** 25582 (2006)
29. Harpham M R et al. *J. Am. Chem. Soc.* **131** 973 (2009)
30. Upton L et al. *J. Phys. Chem. Lett.* **4** 2046 (2013)
31. Varnavski O, Pinsky B, Goodson T (III) *J. Phys. Chem. Lett.* **8** 388 (2017)
32. Guzman A R et al. *J. Am. Chem. Soc.* **132** 7840 (2010)
33. Villabona-Monsalve J P et al. *J. Am. Chem. Soc.* **140** 14562 (2018)
34. Denk W, Strickler J H, Webb W W *Science* **248** 73 (1990)
35. Zipfel W R, Williams R M, Webb W W *Nat. Biotechnol.* **21** 1369 (2003)
36. Helmchen F, Denk W *Nat. Meth.* **2** 932 (2005)
37. Freudiger C et al. *Science* **322** 1857 (2008)
38. Hell S W *Nat. Meth.* **6** 24 (2009)
39. Vogel A et al. *Appl. Phys. B* **81** 1015 (2005)
40. Voronin A A, Zheltikov A M *Phys. Rev. E* **81** 051918 (2010)
41. Voronin A A et al. *Opt. Lett.* **36** 508 (2011)
42. Schrödinger E *What is Life? The Physical Aspect of the Living Cell* (Cambridge: The Univ. Press, 1944); Translated into Russian: *Chto Takoe Zhizn's Tochki Zreniya Fiziki?* (Moscow: RIMIS, 2015)
43. Wawilow S J, Lewschin W L *Z. Phys.* **35** 920 (1926)
44. Vavilov S I *Zh. Russk. Fiz.-Khim. Obshch. Ch. Fiz.* **60** 555 (1928); *Sobranie Sochinenii* (Collected Works) Vol. 1 (Moscow: Izd. AN SSSR, 1954) p. 234
45. Vavilov S I *Die Mikrostruktur des Lichtes. Untersuchungen und Grundgedanken* (Berlin: Akademie-Verlag, 1953); Translated from Russian: *Mikrostruktura Sveta. Issledovaniya i Ocherki* (Micro-structure of Light) (Moscow: Izd. AN SSSR, 1950)
46. Masalov A V, Chizhikova Z A *Phys. Usp.* **54** 1257 (2011); *Usp. Fiz. Nauk* **181** 1329 (2011)
47. Göppert-Mayer M *Ann. Physik* **9** 273 (1931) Vol. 401 on the new numbering of volumes on the site Wiley Online Library
48. Shen Y R *The Principles of Nonlinear Optics* (New York: J. Wiley, 1984)
49. Boyd R W *Nonlinear Optics* (Boston: Academic Press, 1992)
50. Meath W J, Power E A *J. Phys. B* **17** 763 (1984)
51. Albota M et al. *Science* **281** 1653 (1998)
52. Drobizhev M et al. *J. Phys. Chem. B* **110** 9802 (2006)
53. Matsuyama S et al. *Nat. Cell Biol.* **2** 318 (2000)
54. Shu X et al. *Science* **324** 804 (2009)
55. Drobizhev M et al. *J. Phys. Chem. B* **113** 12860 (2009)
56. Drobizhev M et al. *Nat. Meth.* **8** 393 (2011)
57. Filonov G S et al. *Nat. Biotechnol.* **29** 757 (2011)
58. Subach F V, Verkhusha V V *Chem. Rev.* **112** 4308 (2012)
59. Piatkevich K D, Subach F V, Verkhusha V V *Chem. Soc. Rev.* **42** 3441 (2013)
60. Lanin A A et al. *J. Biophoton.* **12** e201800353 (2019)
61. Lanin A A et al. *J. Biophoton.* **13** e201900243 (2020)
62. Lanin A A et al. *Opt. Lett.* **45** 836 (2020)
63. Xu C et al. *Proc. Natl. Acad. Sci. USA* **93** 10763 (1996)
64. Akimov D A et al. *Quantum Electron.* **26** 848 (1996); *Kvantovaya Elektron.* **23** 871 (1996)
65. Akimov D A *Jpn. J. Appl. Phys.* **36** 426 (1997)
66. Boyden E S et al. *Nat. Neurosci.* **8** 1263 (2005)
67. Deisseroth K *Nat. Neurosci.* **18** 1213 (2015)
68. Boyden E S *Nat. Neurosci.* **18** 1200 (2015)
69. Shaner N C, Steinbach P A, Tsien R Y *Nat. Meth.* **2** 905 (2005)
70. Chung I et al. *Nature* **464** 783 (2010)
71. King C et al. *Integr. Biol.* **8** 216 (2016)
72. Molina-Terriza G et al. *Phys. Rev. A* **72** 065802 (2005)
73. Sharping J E et al. *Opt. Express* **12** 3086 (2004)
74. Rarity J G et al. *Opt. Express* **13** 534 (2005)
75. Fulconis J et al. *Opt. Express* **13** 7572 (2005)
76. Fulconis J et al. *Phys. Rev. Lett.* **99** 120501 (2007)
77. Ling A et al. *Opt. Express* **17** 21302 (2009)
78. Cohen O et al. *Phys. Rev. Lett.* **102** 123603 (2009)
79. Medic M et al. *Opt. Lett.* **35** 802 (2010)
80. Petrov N L, Fedotov A B, Zheltikov A M *Opt. Commun.* **450** 304 (2019)
81. Petrovnin K V et al. *Laser Phys. Lett.* **16** 075401 (2019)
82. Russell P *Science* **299** 358 (2003)
83. Reeves W H et al. *Nature* **424** 511 (2003)
84. Zheltikov A M *Phys. Usp.* **43** 1125 (2000); *Usp. Fiz. Nauk* **170** 1203 (2000)
85. Zheltikov A M *Opt. Spectrosc.* **95** 410 (2003); *Opt. Spektrosk.* **95** 440 (2003)
86. Akimov D A et al. *Opt. Lett.* **28** 1948 (2003)
87. Zheltikov A *J. Opt. Soc. Am. B* **22** 1100 (2005)
88. Zheltikov A M *Phys. Usp.* **47** 69 (2004); *Usp. Fiz. Nauk* **174** 73 (2004)
89. Ortigosa-Blanch A et al. *Opt. Lett.* **25** 1325 (2000)
90. Kerbage C et al. *Opt. Lett.* **27** 842 (2002)
91. Hu M L et al. *Opt. Express* **12** 1932 (2004)
92. Zheltikov A M *Opt. Commun.* **252** 78 (2005)
93. Mitrofanov A V et al. *Opt. Express* **14** 10645 (2006)
94. Petrov N L et al. *Appl. Phys. B* **125** 54 (2019)
95. Garay-Palmett K et al. *Opt. Express* **15** 14870 (2007)
96. Law C K, Walmsley I A, Eberly J H *Phys. Rev. Lett.* **84** 5304 (2000)
97. Parker S, Bose S, Plenio M B *Phys. Rev. A* **61** 032305 (2000)
98. Snyder A W, Love J D *Optical Waveguide Theory* (London: Chapman and Hall, 1983)
99. Marcuse D *J. Opt. Soc. Am.* **68** 103 (1978)
100. Mortensen N A et al. *Opt. Lett.* **28** 1879 (2003)
101. Zheltikov A M *JETP Lett.* **91** 378 (2010); *Pis'ma Zh. Eksp. Teor. Fiz.* **91** 410 (2010)
102. Akimov D A et al. *Appl. Phys. B* **74** 307 (2002)
103. Leon-Saval S G et al. *Opt. Express* **12** 2864 (2004)
104. Zheltikov A M *Phys. Usp.* **49** 605 (2006); *Usp. Fiz. Nauk* **176** 623 (2006)
105. Zheltikov A *J. Opt. Soc. Am. B* **36** A168 (2019)
106. Bernstein J G, Garrity P A, Boyden E S *Curr. Opin. Neurobiol.* **22** 61 (2012)
107. Bath D E et al. *Nat. Meth.* **11** 756 (2014)
108. Chen R et al. *Science* **347** 1477 (2015)
109. Fedotov I V et al. *Sci. Rep.* **5** 15737 (2015)
110. Lanin A A et al. *Opt. Lett.* **41** 5563 (2016)
111. Ermakova Y G et al. *Nat. Commun.* **8** 15362 (2017)
112. Doronina-Amitonova L V et al. *Phys. Usp.* **58** 345 (2015); *Usp. Fiz. Nauk* **185** 371 (2015)